

Regular article

Simona Ungureanu, Branko Kolaric, Jianing Chen, Rainer Hillenbrand
and Renaud A. L. Vallée*

Far-field disentanglement of modes in hybrid plasmonic-photonic crystals by fluorescence nano-reporters

Abstract: In this paper, the resonance modes exhibited by a hybrid nanostructure have been disentangled in the far-field owing to narrow-band fluorescence nano-reporters. Hybrid plasmonic-photonic crystals were fabricated using large (457 nm) monodisperse polystyrene spheres self-assembled into 2D photonic crystals and subsequently coated by a 30 nm thick silver layer. Such structures exhibit a complex resonance pattern, which has been elucidated owing to numerical simulations and electric near-field patterns obtained with a scattering type scanning near-field optical microscope (s-SNOM). For the sake of disentangling the resonance modes of the hybrid structure in the far-field, different types of semiconductor quantum dots (QDs), acting as nano-reporters of the local interactions, were dispersed on top of distinct structures. Depending on the relative overlap of the emission spectrum of a particular type of QDs with the resonance features of the hybrid structure, we affect their emission rate in a unique way, as a consequence of the complex interaction occurring between the plasmo-photonic modes and the excitons. Such plasmonic structures appear to be particularly relevant for fluorescence-based sensing devices.

Keywords: plasmonic crystal; fluorescence lifetime; surface plasmon resonance; Bloch modes; Purcell effect.

PACS number: 73.20.Mf

*Corresponding author: Renaud A. L. Vallée, CNRS, University Bordeaux, CRPP, UPR 8641, F-33600 Pessac, France, e-mail: vallee@crpp-bordeaux.cnrs.fr

Simona Ungureanu: CNRS, University Bordeaux, CRPP, UPR 8641, F-33600 Pessac, France

Branko Kolaric: Laboratoire Interfaces and Fluides Complexes, Centre d'Innovation et de Recherche en Matériaux Polymères, Université de Mons, 20 Place du Parc, B-7000 Mons, Belgium

Jianing Chen: CIC nanoGUNE Consolider, 20018 Donostia – San Sebastián, Spain

Rainer Hillenbrand: CIC nanoGUNE Consolider, 20018 Donostia – San Sebastián, Spain; and IKERBASQUE, Basque Foundation for Science, 48011 Bilbao, Spain

Edited by Niek van Hulst

1 Introduction

Noble metal nanostructures strongly modify the emission rate of quantum emitters (fluorophores, quantum dots QDs) placed in their vicinity [1–9], due to the interaction between excitons and surface plasmon polaritons (SPPs). These SPPs, which are collective oscillations of the conduction electrons of a metal surface coupled to the electromagnetic field that initiated the excitation, can either be localized (LSPPs) as e.g., for metal nanoparticles of various sizes and shapes or delocalized (SPPs) as e.g., for thin metal films [10].

A periodically nanostructured noble metal obtained by combining a continuous metal film to a dielectric photonic crystal both supports SPPs and LSPPs and allows to control the interplay between them [11]. Furthermore, the coupling strength between the photonic and plasmonic components of such a hybrid structure is strongly increased if the plasmonic component possesses its own resonances, one/some of them overlapping the resonances of the photonic crystal [12]. In particular, hybrid structures obtained by nanosphere lithography [13] and consisting of ordered arrays of metal half-shells vapor-deposited in thin films (thickness of the order of 20–30 nm) on top of 2D colloidal crystals (2D CC) used as substrates present interesting optical properties [14, 15]. Owing to the corrugated metal surface, SPPs are diffractively coupled to the incident and transmitted light and LSPP resonances can also be excited. The transmission spectra through such a hybrid structure have been shown to be quite similar to those observed through subwavelength hole arrays in metal films [16–18]. The close spectral correspondence between transmission peaks in the metal coated 2D CC and transmission dips in the uncoated 2D CC pointed to the possible relevance of guided (Bloch) modes in the hybrid structure. Guided (Bloch) modes and cavity resonances of all dielectric 2D CC become more pronounced due to stronger light localization in the metal terminated

diffraction gratings. This relevance was corroborated by the computed electromagnetic field distributions, which present strong field confinement at the location of the spheres, both within the sphere and near the metal external boundary, evidencing the occurrence of a Bloch-SPP mode at the transmission maximum [11, 19]. Recently, an emission enhancement of 28 times was demonstrated for fluorophores placed at about 1 nm above the hybrid structure [20]. The enhancement was shown to be correlated with the spectral overlap of the fluorophore emission and the Bloch-SPP mode of the hybrid structure, indicating a surface plasmon-coupled emission mechanism for the enhancement.

The different types of resonances originating from the coupling of plasmonic and photonic modes in hybrid structures may differently influence the emission properties of quantum emitters spectrally overlapping one or the other of these resonances. Investigating the richness of modes in such structures is of particular fundamental interest and time-resolved measurements certainly are to play a major role in disentangling the contributions of different enhancement pathways [8, 9, 21].

Furthermore, plasmonics generally offers the opportunity to develop ultra-sensitive bioassays for the analysis of various complex biomedical and environmental samples including body fluids, food and soil [22, 23]. One of the biggest challenges is rapid detection at low concentrations of proteins, DNA structures and microbes. The coupling nanoprobe emission response with plasmonic and hybrid plasmonic/photonic excitations in complex environments such as hybrid photonic plasmonic structures offers a pathway to develop such critically needed technologies.

In this paper, we conceptually present and experimentally demonstrate how the emission rates of quantum dots (QDs) dispersed on a hybrid structure can either be controlled by- or be exquisite sensors of the nanoscale interactions between the excitons and the plasmo-photonic modes of the structure. This investigation could be performed owing to the use of narrow-band emission nano-reporters perfectly overlapping the hybrid modes of interest. Specific wavelength-shaped rates enhancements have been observed, which are explained, on the base of numerical simulations, as due to the coupling strength between the involved modes and the QDs excitons.

2 Materials and methods

Latex microspheres [diameter $D=0.457\ \mu\text{m}$, 2.5% solids (w/v) aqueous suspension] were supplied by Polysciences.

Ag (99.999% 1–3 mm) was purchased from Aldrich. CdSe@ZnS quantum dots in water with emission color green (520–550 nm), orange (590–615 nm) and dark red (640–660 nm) were supplied by NN-Labs. CdSe@ZnS quantum dots in toluene with emission peaks at 590 nm and 640 nm were supplied by Aldrich.

Glass plates with a size of $2\times 2\ \text{cm}^2$ and a thickness of 5 mm were carefully cleaned and treated with UV-ozone for 30 min. Then an opportune ratio of Triton $10^{-3}\ \text{M}$ in water/polystyrene (PS) microspheres was deposited on the glass surface and dried under a tilt angle of approximately 10° under controlled conditions of temperature and humidity ($T=293\ \text{K}$, $H=65\%$). After formation of large areas of well ordered monolayers of latex nanospheres, the substrates were covered with 30 nm of silver using standard evaporation techniques, the thickness being controlled by an in-situ mounted quartz crystal microbalance (QCM). Then a 20 μl volume of QDs solution (1% v/v in either water or toluene/ethanol) were spread on the silver coated monolayers.

Scanning electron micrographs (SEM) were recorded on a field-emission scanning electron microscope (FESEM, JEOL JSM-6700F).

The absorbance spectra of the plasmonic-photonic crystals were measured on the whole visible spectrum by performing total integrated forwards transmission, owing to a white light illumination lamp (fiber coupled white light HL-2000-HP-FHSA, Ocean Optics) used in combination with an integrating sphere (fiber coupled integrating sphere FOIS-1, Ocean Optics) and a spectrometer (fiber spectrometer USB2000+VIS-NIR, Ocean Optics). The areas illuminated were of the order of $(3\ \text{mm})^2$.

The spontaneous emission properties of the various quantum dots were recorded with a spectral- and time-resolved setup consisting of a streak camera (HAMAMATSU Streak Scope C10627) pre-fitted with a spectrograph (Princeton Instruments) with a 150 g/mm choice of the grating. The excitation light was the frequency doubled output of the $\lambda=1030\ \text{nm}$ wavelength, 10 MHz repetition rate, 300 fs line width pulses delivered by a diode-pumped Ytterbium femtosecond oscillator from Amplitude systems (t-Pulse 200). The beam was collimated to a 3 mW, 5 mm diameter spot to excite the emitters in the targetted nanostructure prior to focus the 530 nm long-pass filtered emission intensity on the entrance slit of the spectrograph.

The scattering-type scanning near-field optical microscope (s-SNOM) used in this work is based on an atomic force microscope (AFM) that uses cantilevered tips as near-field probes (NeaSNOM from Neaspec GmbH) [24]. For imaging near-field distributions we use standard

commercial Si tips (Arrow tip, NanoWorld). The tip oscillates at the mechanical resonance frequency $\Omega \approx 300$ kHz with an amplitude $\Delta \approx 30$ nm, while the sample is scanned. A laser beam ($\lambda = 633$ nm) is focused to the tip apex using a parabolic mirror. The backscattered light is analyzed with a pseudo-heterodyne Michelson interferometer, yielding both the amplitude E and phase ϕ of the backscattered light [24]. Background contributions are suppressed by demodulating the detector signal at a harmonic frequency $n\Omega$ ($n \geq 2$), yielding background free near-field amplitude and phase images. In order to avoid distortion of the plasmon modes by near-field coupling between the hybrid structure and the tip, we illuminate the sample with s-polarized light. In this scheme, the incident light efficiently polarizes the hybrid structures but not the AFM tip [25–27]. In the presented experiments, the p- and s-polarized backscattered light is selected by a vertically or horizontally aligned polarizer in front of the detector, respectively. To achieve interference between the s-polarized incident light and the detected p-polarized backscattered light, a 45° rotated polarizer is placed in between the reference mirror and the beam splitter.

The transmission spectra and various modes of the hybrid structure have been simulated by solving Maxwell equations using the three-dimensional finite-difference time-domain (FDTD method) [28], as implemented in the freely available MEEP software package [29]. By Fourier-transforming the response to a short, broadband, spatially extended gaussian pulse in the near-field of the passive structures and normalizing with the response in vacuum for the same excitation conditions, a single simulation yielded the transmission spectra over a wide spectrum of frequencies. The resonance modes were obtained by sending a narrowband, at the wavelength of interest, spatially extended gaussian pulse in the near-field of the structure and recording the three components of the electric field in time. Finally, in order to compute the (total and radiative) spontaneous emission rate enhancements of the emitters in the nanostructures, we performed Fourier-transforms of the response to a short, broadband, point dipole (electric current) gaussian pulse polarized along either the X- or Z-axis (Figure 3). We then normalized this response with the one obtained for a point dipole located close to the substrate in the same excitation conditions. In all types of simulations, the electric field propagates along Z (Figure 3); periodic boundary conditions were implemented in the X and Y directions while perfectly matched layers (PMLs) were implemented in the propagation direction. The dielectric permittivities of the glass substrate and the PS spheres were taken as 2.3 and 2.5, respectively. The dielectric permittivity of gold was specified by using a

sum of Drude and Drude-Lorentz terms, according to the work performed by Rakic et al. [30]. To simulate at best the spontaneous emission rate of the emitters in the structures, we represented these emitters (CdSe/ZnS QDs) as small spheres of 5 nm diameter with a dielectric constant of 5.76 (the dielectric constant of the ZnS shell), the point dipole source being located at the center of this sphere.

3 Results and discussion

3.1 Modes of the hybrid structure

Three types of substrates have been prepared and investigated in order to differentiate the effect of the hybrid structure on the emission behaviour of QDs later deposited on top of the structures. Figure 1 (left) exhibits the scheme of the various designs. In step I, a dispersion of QDs is directly deposited onto a glass substrate. In step II, the glass substrate has been covered by a 30 nm thick silver film, owing to metal vapor deposition, prior to drop cast the QDs dispersion. Finally, in step III, a monolayer of PS spheres of $D = 457$ nm diameter has been hexagonally self-assembled onto the glass substrate, prior to deposit a 30 nm thick corrugated silver film followed by the drop casting of the QDs dispersion.

A top-view scanning electron microscope (SEM) image at two different magnifications is presented in Figure 1 (right), exhibiting the exceptionally good ordering of the self-assembled hybrid structure on small and large scales. Typically, the monolayers exhibit a polycrystalline structure with a typical domain size of about 50–100 μm . Note that the small scale micrograph here shows an essentially single crystalline domain, presenting small disruptions, unavoidable due to the small polydispersity in size of the spheres and the employed drying procedure, which do not alter the orientation of the adjacent zones.

Figure 2A exhibits typical transmission spectra at normal incidence of the hybrid structure (solid black line) and of a flat silver film of the same nominal thickness for reference (dashed black line). The flat film exhibits the well-known characteristics of a semi-transparent film, being rather opaque in the visible range. On the contrary, the optical spectrum of the hybrid structure is significantly structured. The overall transmission is strongly increased as compared to the transmission of the flat silver film, and exhibits well-defined maxima and minima. A main maximum with an asymmetric profile, reaching 31% transmittance, is centered around 640 nm. These spectral features (strong maxima and minima, and

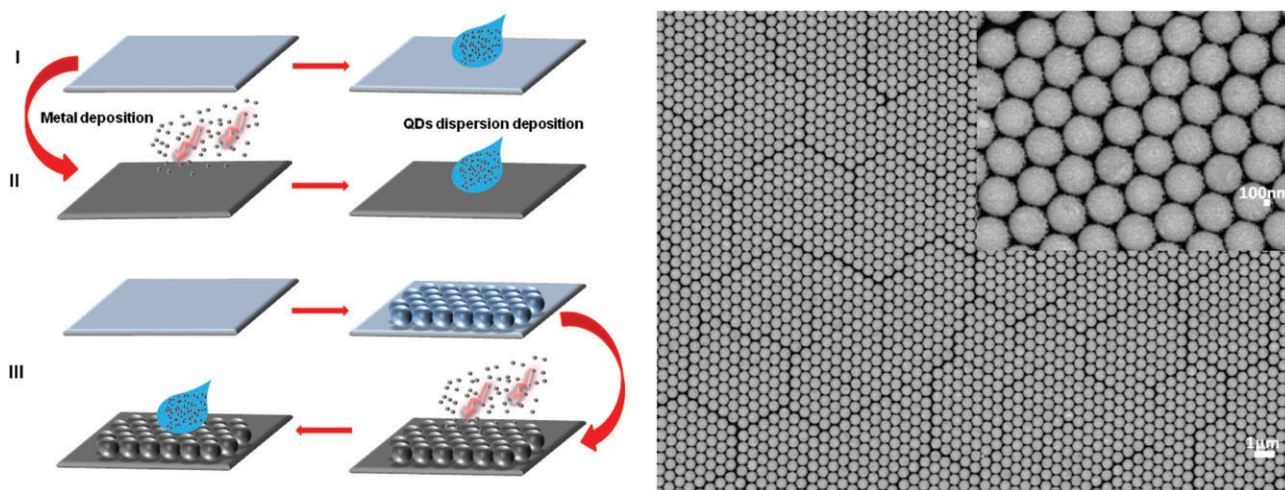


Figure 1 Left: Schemes of the structures' designs. In step I, QDs are directly dispersed from the solution onto the glass substrate. In step II, silver is vapor deposited on the glass substrate prior to disperse the QDs on top. In step III, a 2D colloidal crystal (2D CC) of polystyrene spheres is self-assembled on the glass substrate prior to perform silver vapor and QDs dispersion depositions to realize the hybrid plasmo-photonic (hybrid) structure. Right: SEM top views of the hybrid structure at two different magnifications.

peak asymmetry) resemble very much those previously reported for extraordinary transmission on metallic sub-wavelength hole arrays [19].

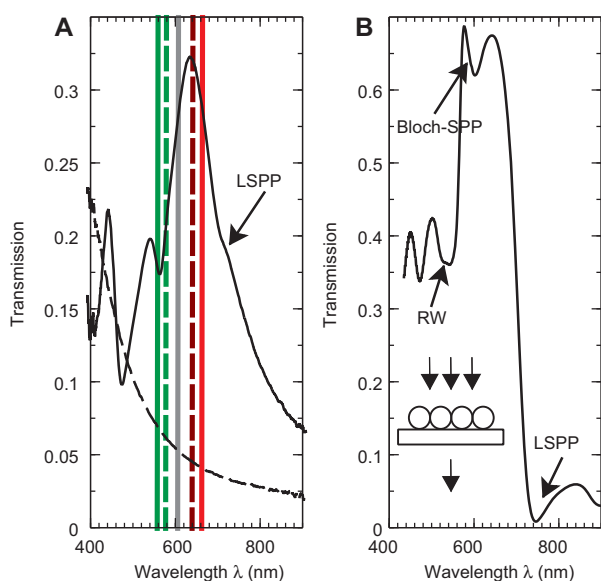


Figure 2 Experimental (A) and numerical (B) transmission spectra of the hybrid structure (solid black line) and the flat silver film (dashed black line). The wavelength of the various QDs emission maxima in solution are also shown in a: Ems-g2, Ems-o and Ems-r2 QDs are depicted in green, gray and red solid lines while Ems-g1 and Ems-r1 QDs are in dark green and dark red dashed lines, respectively. Bloch-SPP, RW and LSPP denote the combined Bloch-Surface Plasmon Polariton mode, the Rayleigh-Wood mode and the Localized Surface Plasmon Polariton mode. The inset shows the numerical conditions of excitation and detection of light in the hybrid structure.

According to the recently published literature [11, 12, 18], the transmission peak maximum, here located at 640 nm, is attributed to a Bloch-SPP mode. The Bloch mode wavelength is given by $\lambda_{max} = 2\pi n_{eff} / G_{kl}$, where n_{eff} is the effective refractive index of the PS array and $G_{kl} = 4(\pi / \sqrt{3D}) \sqrt{k^2 + l^2} + kl$ is a reciprocal vector of the grating. The large electromagnetic field intensity achieved due to the field confinement in a Bloch mode promotes the excitation of SPPs, which are coupled out. The transmission minimum found on the short-wavelength side of the main transmission peak is associated to light diffracted parallel to the lattice surface, and is known as Wood anomaly or Rayleigh-Wood (RW) anomaly [11, 31]. Another resonance in the metal-on-monolayer hybrid structure refers to localized plasmons excited in individual half-shells (HSs) [12]. Isolated silver HSs were shown to exhibit transverse (polarized parallel to the half-shell symmetry axis) and longitudinal plasmon resonances [32]. By joining these HSs in a dense array, the longitudinal mode is suppressed. A strong plasmon excitation manifests itself through a strong absorption of incident light. The inflection point around 705 nm, exhibited in the transmission spectrum of Figure 2A and considerably red-shifted with respect to the transmission maximum, might be attributed to localized surface plasmon polariton (LSPP) resonances in the silver half-shells, which are coupled and strongly interacting at the HS rim junctions of the hybrid structure [11, 32].

In order to get an in-depth insight of the modes involved in the complex pattern exhibited in Figure 2A, we performed numerical (FDTD) simulations of the

hybrid structure. In a first step, the transmission spectrum of the metal corrugated surface has been simulated at normal incidence. Figure 2B shows the calculated spectrum, which is similar, while with some added features, to the experimentally obtained one. The dip observed in Figure 2A on the short wavelength side of the main transmission peak is still clearly present at $\lambda=535$ nm (RW). At $\lambda=745$ nm, a strong dip clearly substitutes to the inflection point in Figure 2A, which better points to a LSPP resonance. One could attribute the observation of the inflection point in Figure 2A instead of the minimum in Figure 2B as due to the averaging of the transmitted signal caused by the structural defects in the real sample. Another type of averaging is experimentally performed: the experimental transmission spectrum is integrated over all transmitted angles, for a normal incidence of the excitation light, while the detection is performed numerically at normal incidence. This explains the differences observed in the absolute transmittances. The short wavelength peaks (below and around 500 nm), possibly due to re-mappings (via a reciprocal lattice vector) of the fundamental Bloch mode or to higher guided modes [19], are noticeable for both numerical and experimental results. Interestingly, a double-feature now appears in the main peak of the calculated transmission spectrum, with a crest-dip-crest succession at the wavelengths of 577 nm, 602 nm and 643 nm. This double-feature appearing in the calculated transmission spectrum was in fact noticed in angularly resolved transmission experiments [11], where the splitting of two modes, the existence of which was attributed to the dielectric asymmetry in the out of plane direction of the structure [33], increased with the incidence angle.

In a second step, the electric near-field patterns of the modes of interest have been calculated. Their E_x and E_z components are shown in Figure 3. In this figure, light is

propagating along Z axis, i.e., in the vertical direction from bottom to top and is polarized along X direction. Positive and negative values of the field are related to the orientation of the electric field vector with respect to the axes.

The mode at $\lambda=535$ nm exhibits rather peculiar features. A significant part of the E_x component of the electric field traverses the structure and exhibits a transmitted field distribution seemingly originating from an interference mechanism. The E_z map further reveals a doubly periodic pattern, in the X and Z directions, indicative of a propagative mode with z-polarized light propagating in the XZ plane. These features strongly point to the observation of light diffracted by the lattice surface. The position of this minimum in the transmission spectrum indicates the wavelength above which free space light diffraction is forbidden for the given order. This mode is thus clearly ascribed to a Rayleigh-Wood (RW) anomaly.

At $\lambda=577$ nm, we observe considerable E_x and E_z components of the electric field. The E_x component indicates that a large part of the incident x-polarized light is directly transmitted through the structure. The field distribution further suggests that an interference mechanism could contribute to the transmission band. The E_z map exhibits a periodic pattern in the X direction, indicative of a propagative mode in the plane of the array, with z-polarized light propagating along X. The distance between two lobes, which is roughly a sphere radius, together with the large spatial extension, support the propagative nature of this mode. The same E_z map reveals a symmetric coupling between the outer and inner surfaces of the half-shell, again characteristic for long-range propagative modes. These features support the Bloch-SPP nature of the mode, already firmly attributed by Romanov et al. as a consequence of (i) the polarization anisotropy observed in transmission for such a hybrid structure and (ii) the spectral overlap of the index guided modes with SPP waves,

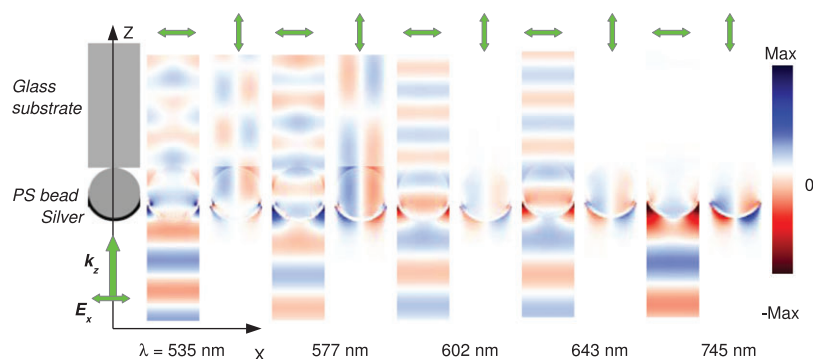


Figure 3 Electric near-field patterns of the Rayleigh-Wood (RW, 535 nm), Bloch-SPP (577 nm), short-range SPPs (602 nm, 643 nm) and localized surface plasmon polariton (LSPP, 745 nm) modes calculated owing to FDTD simulations. In these simulations, the exciting electric field, polarized along X, propagates along Z, and is detected in the X (E_x) and Z (E_z) directions close to the hybrid structure.

similar to that observed in a perforated metal film, established in the dispersion relation of the hybrid structure [12].

The electric near-fields patterns shown at $\lambda=602$ nm and $\lambda=643$ nm are very similar and exhibit a peculiar evolution when compared to the Bloch-SPP mode just discussed. A large part of the incident x-polarized light is still directly transmitted through the structure. However, this x-polarized transmitted field does not prefigure any interference pattern anymore. Furthermore, the z-component of the electric field is confined to the sphere and its incident boundary, with an asymmetric coupling between the outer and inner surfaces of the half-shell. Such features point to a short-range SPP nature of the modes [34], associated with a dip in transmission at $\lambda=602$ nm. This wavelength might thus also signal a decoupling from the Bloch mode.

At $\lambda=745$ nm, the E_x component of the electric field, contrary all previous cases, does not penetrate into the structure, being instead trapped at the junction between silver half-shells. Both E_x and E_z fields are very strongly localized, and appear to be focussed at the V-shaped groove between two half-spheres rims. The structure of the fields on each side of a half-shell, with spatial extension decreasing and enhancement increasing from the top towards the rim, is reminiscent of the one of tapered tips [35]. The E_z map further reveals a strong asymmetric coupling between the outer and inner surfaces of the half-shell, a rather specific feature of short-range plasmons. These observations allow us to confirm the assignment of this mode to a localized surface plasmon polariton (LSPP) resonance. Let us note here that, besides reports in the literature [11, 32], the attribution of the inflection point in Figure 2A to a LSPP is based on comparison with Figure 2B, the latter being confirmed by the electric field pattern observed in Figure 3.

Similar EM field maps were previously reported for the Bloch-SPP mode and the LSPP resonance [11, 19]. Here, we further provide a rather complete description of the RW anomaly in such a hybrid structure and some hints about the existence of a short-range SPP mode decoupled from the Bloch mode in the transmission maximum.

Our assignment of the various resonance modes is established on the basis of a comparison between experimentally and numerically obtained transmission spectra followed by numerical simulations of the modes' field patterns. Very interestingly, all field profiles appear to be tightly focussed at the V-shaped groove between the half-shells, a situation highly favorable to the enhancement of the emission properties of QDs there deposited. In order to better quantify these observations and certify the "reality" of the numerically obtained field patterns, we

proceeded to two further investigations. On the numerical side, we calculated the Purcell factor $F(\vec{r}_0, \omega) = \frac{P_t(\vec{r}_0, \omega)}{P_0(\vec{r}_0, \omega)}$ describing the spontaneous emission rate enhancement of an emitter in a dedicated electromagnetic environment, where $P_t(\vec{r}_0, \omega) = \frac{\omega}{2} \text{Im}(\vec{p} \cdot \vec{E}(\vec{r}_0))$ and $P_0(\vec{r}_0, \omega)$ are the total power dissipated by an infinitesimal oscillating dipole \vec{p} located at \vec{r}_0 in the hybrid structure and close to the dielectric bare substrate, respectively [36]. On the experimental side, we measured the near-field pattern of a short-range SPP mode of the hybrid structure with a scattering-type scanning near-field optical microscope (s-SNOM).

The broadband Purcell factors for either a x-polarized emitter located in the V-grooves between the half-shells (dashed line) or a z-polarized emitter located in front of the center of a sphere (dotted line), 5 nm away from the metal boundary on the air side are shown in Figure 4. Emitters in close proximity of a metal nanostructure experience non-radiative (ohmic) losses. The total spontaneous emission rate is the sum of the radiative and non-radiative rates, the latter being dominant in most metal nanostructures [3, 6, 8, 9]. Accordingly, the radiative parts (solid lines) of the Purcell Factors, calculated in the far field of the structures, are also shown in Figure 4. Clearly, the Purcell factors F exhibit specific signatures of the underlying resonances modes with local maxima found around 510 nm, 600 nm and 700 nm. It is remarkable to observe that the Purcell factor is essentially large, featuring a spontaneous emission rate enhancement of possibly 4 orders of magnitude for an emitter located in close proximity of the hybrid structure as compared to the same emitter close to the bare dielectric substrate. As suggested by the tight focusing of the fields in the V-shaped grooves between the HSs (Figure 3), the Purcell factor is essentially much larger at all wavelengths for an x-polarized emitter located at this position as compared to a z-polarized emitter located in front of the HS (Figure 4, the polarization of the emitter at these two positions is normal to the HS boundaries, a situation that is well known to lead to an optimized coupling between the dipole and the plasmon resonances).

Near-field imaging of the short-range SPP mode was performed with a s-SNOM [37] at $\lambda=633$ nm wavelength with s-polarized light under an oblique incidence angle of 30° . Being equipped with a pseudo-heterodyne interferometric detection scheme [24], the microscope allows for mapping both the amplitude E and phase ϕ of the electric near-field x-component (parallel to the sample surface) and z-component (normal to the sample surface) at the hybrid structure surface. The combined information of

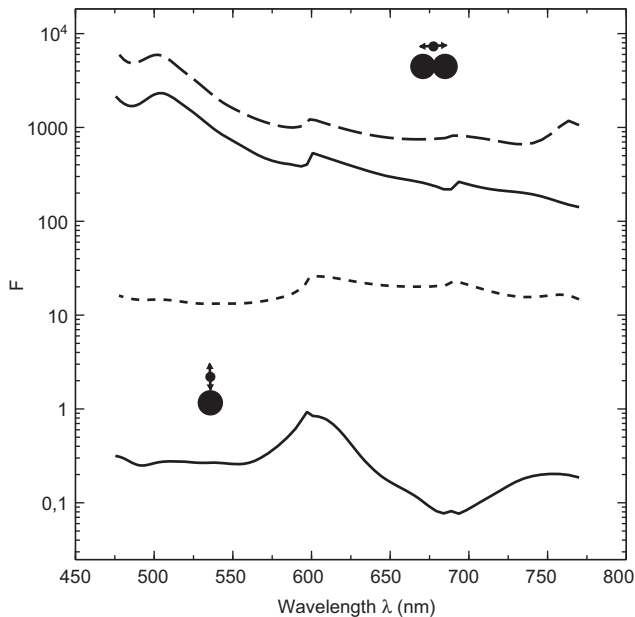


Figure 4 Purcell factor as a function of wavelength for either an x-polarized emitter located in the V-grooves between the half-shells (dashed line) or a z-polarized emitter located in front of the center of a sphere (dotted line), 5 nm away from the metal boundary on the air side. The radiative Purcell factors are also shown as solid lines below the dashed and dotted lines for an x-polarized/z-polarized emitter, respectively.

amplitude and phase of the z-component provides a qualitative description of the surface charge density distribution associated with the mode oscillations [37].

Figure 5A shows the topography of the hybrid structure, revealing the nice hcp configuration of the spheres in the monolayer at very large magnification. Figure 5B provides experimental evidence of a short-range SPP mode in the structure with the measured x- and z-components of the real part $E_{\cos(\phi)}$ of the electric field vector. Clearly noticeable on the figure are the lobes signaling the large field amplitudes. These lobes have the same phase for the x-component of the electric field while there is a π phase jump between the lobes in the case of E_z . Furthermore, the spacing between the E_x lobes is clearly larger than the one between the E_z lobes. These features are in excellent agreement with the simulations shown in Figure 5C, realized by recording the electric field pattern 15 nm above the corrugated surface raster scanned in a way similar to the s-SNOM tip, after excitation with a s-polarized light under an oblique incidence angle of 30° . By comparing both experimental and numerical near-field patterns with the short-range SPP mode ($\lambda=643$ nm) exhibited in Figure 3, it is clear that the large (small) interdistance and the $0(\pi)$ phase jump between the lobes for the x- (z-) component of the electric field are fully compatible. Furthermore,

contrarily to the LSPP resonance at 745 nm, the x-component of the electric field also presents a π phase jump in between the lobes (Figures 3 and 5). Together with the transmission measurements performed elsewhere [11] at oblique incidence, indicating only a slight red shift of the peak at 643 nm for a 30° incidence angle, these observations confirm the attribution of the short-range SPP to the mode pattern shown in Figure 5. Furthermore, the confinement of the x-component of the electric field in the V-shaped grooves between the HSs is experimentally demonstrated, which should favor the emission enhancement of emitters there located.

3.2 Fluorescence nano-reporters of the modes in the hybrid structure

Having elucidated the origin of the resonance modes in the hybrid structure, we now aim to show that a far-field measurement can disentangle these modes in a unique way, owing to narrow-band fluorescence emitters dispersed on top of the structure, which experience and report on the coupling strength of their near-field

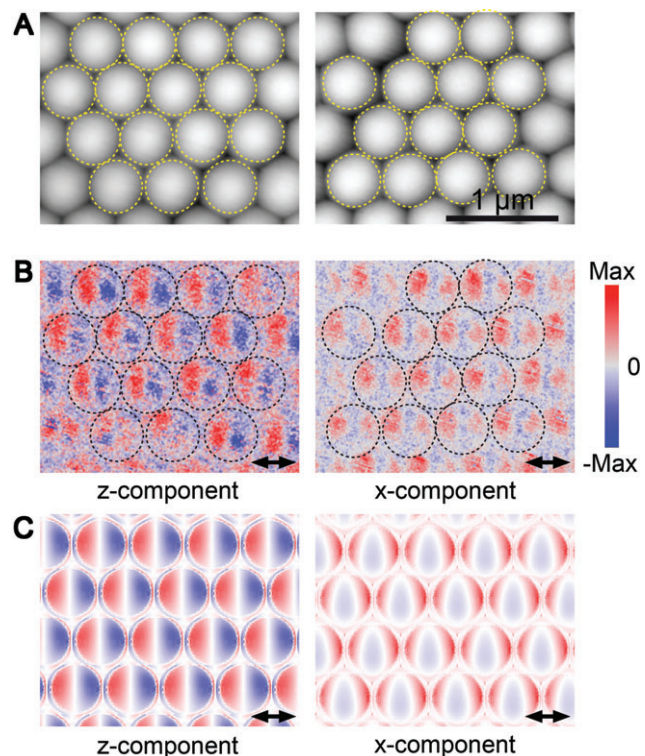


Figure 5 AFM amplitude (A) and real part of the x- and z-components of the electric near-field of the HP mode (B) measured at $\lambda=633$ nm with a s-SNOM. (C) FDTD calculated near-field patterns of the hybrid structure in the conditions of the s-SNOM measurement. The black arrows, in (B,C), indicate the in-plane polarisation of the incident field.

interactions with the plasmo-photonic modes of the structure. Five types of CdSe@ZnS QDs are here investigated. Two of them (Ems-g1 and Ems-g2, Figure 1) are chosen to emit in the green part, in the wavelength range at and between the RW and the Bloch-SPP modes. A third one (Ems-o) emits in the wavelength range of the Bloch-SPP mode. The last two (Ems-r1 and Ems-r2) are chosen to emit in the red part of the visible spectrum, in the wavelength range covering the SPPs modes, towards the LSPP resonance. A further distinction between these QDs is that Ems-g2, Ems-o and Ems-r2 have a large ligand overlayer grafted on the Core-Shell semiconductor nanostructure, notably allowing one to make them soluble in water, while Ems-g1 and Ems-r1 do not. As a result of this large ligand overlayer, the Ems-g2, Ems-o and Ems-r2 QDs are spaced further away to the underlying structure than the Ems-g1 and Ems-r1 QDs.

First of all, in order to check whether the deposition of such QDs on the plasmonic structure does not alter the optical properties of the structure, we performed all-angles integrated transmission spectra of the doped structures. Figure 6 shows these spectra. The main resonance features described here above are still clearly observed and, more importantly, are only slightly spectrally dispersed

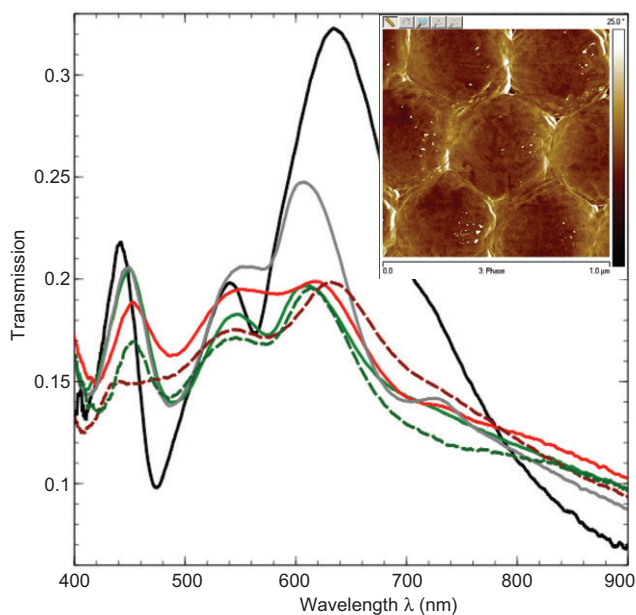


Figure 6 Experimental transmission spectra of the doped hybrid structures. Structures on which Ems-g2, Ems-o and Ems-r2 QDs have been deposited are depicted in green, grey and red solid lines while Ems-g1 and Ems-r1 QDs are in dark green and dark red dashed lines, respectively. The black curve is the transmission spectrum of the reference hybrid structure. The inset shows an AFM phase image exemplifying the locations of the QDs (white spots) deposited on top of the structure.

with respect to the original structure. Noting that each of the hybrid structures have already small intrinsic spectral shifts due to fabrication uncertainties, the presence of the QDs clearly has a negligible effect on the optical properties of the structure. The inserted AFM phase image further exemplifies the locations taken by these QDs on top of the structure. The low concentration used in the deposition procedure results in a dilute dispersion of the QDs on top of the structure, which excludes a major distortion of the resonance properties of the structure.

Since the quantitative determination of emission enhancement based on fluorescence intensities near a metal surface is prone to major errors related to the difficulty of properly taking into account notably (i) the number of emitters grafted to the surface; (ii) the excitation and collection efficiencies of the setup and (iii) the spatial pattern of emission due to the coupling with the plasmonic antenna [38], we focused in this study on the measurement of spontaneous decay rates as a function of wavelength. Indeed, the spontaneous decay rate of a quantum emitter is a direct observable of the intrinsic properties of the emitters and of their eventual coupling with their surrounding, notably through the Purcell factor. This observable does not depend on the number of emitters (as far as the latter are not aggregated) and on the experimentally used geometry. Furthermore, through this observable, the quantum emitters emit fluorescence in the far-field while reporting on interactions occurring in the near-field, thus acting as nanoscale reporters of the local interactions.

We have measured the decay rates of quantum emitters embedded in the various nanostructures by performing simultaneous spectrally and temporally resolved measurements, owing to the use of a streak camera. Figure 7 exhibits spectro-temporal intensity streak plots of the Ems-r2 QDs dispersed from the aqueous solution directly onto either the glass substrate (left) or the hybrid structure (right). By projecting the intensity on the y axis, one obtains decay rates profiles, with significantly shortened decay times as the investigated QDs are dispersed on the hybrid structure (Figure 7, right).

We investigated the emission properties as a function of wavelength, building the decay profiles for all samples by dividing the wavelength range in 20 regions of 4 nm width and proceeded to fitting of these decay profiles. Figure 8 shows three decay profiles of the Ems-r2 QDs in 4 distinct environments. The four environments are QDs in solution (A), dispersed on the glass substrate (B), dispersed on the silver coated glass substrate (C) and dispersed on the hybrid structure (D). The three profiles correspond to sub-wavelength regions located 20 nm on the short-wavelength side (red circle), at the wavelength

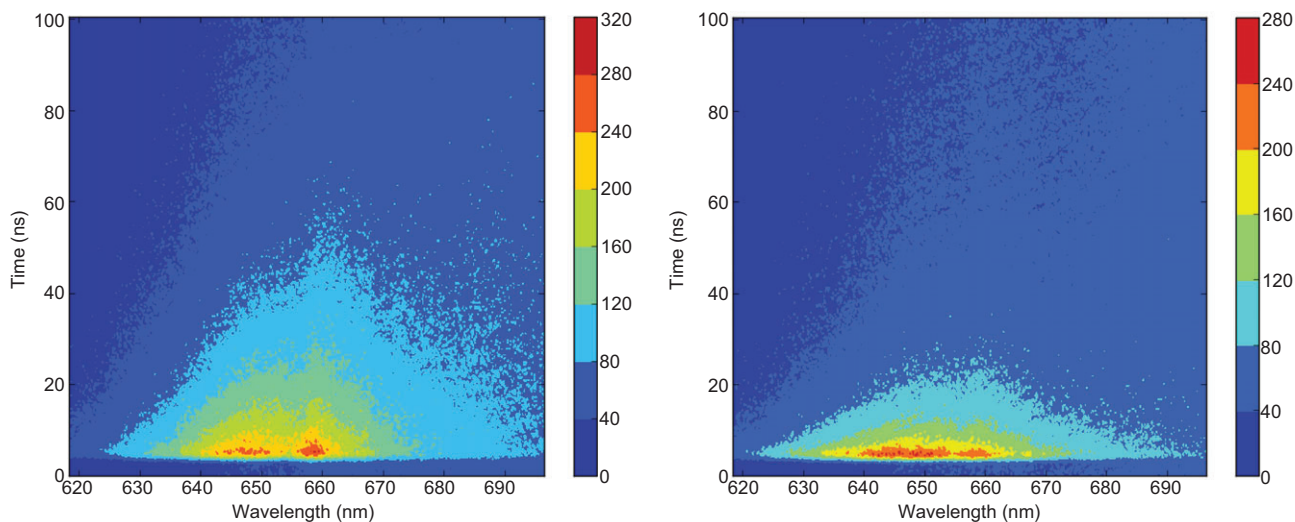


Figure 7 Time and spectrally resolved spontaneous emission intensities (streak plots) of Ems-r2 QDs dispersed on either the glass substrate (left) or the hybrid structure (right).

(green left triangle) and on the long-wavelength side (blue right triangle) of the maximum emission.

On the one side, the decay profiles of the Ems-r2 in ethanol (A) and on a glass substrate (B) show an essentially single exponential decay profile with a decay time increasing as a function of wavelength. In solution, Ems-r2 has a decay time ranging from 11 ns at $\lambda=630$ nm to 52 ns at

$\lambda=685$ nm. On the other side, the decay profiles slightly (C) and strongly (D) deviate from a single exponential decay profile as the QDs are dispersed on the silver coated glass substrate and on the hybrid structure, respectively. In the hybrid structure, Ems-r2 has a decay time ranging from 4 ns at $\lambda=630$ nm to 13 ns at $\lambda=685$ nm. In order to fit such decay profiles adequately, we used a stretched exponential

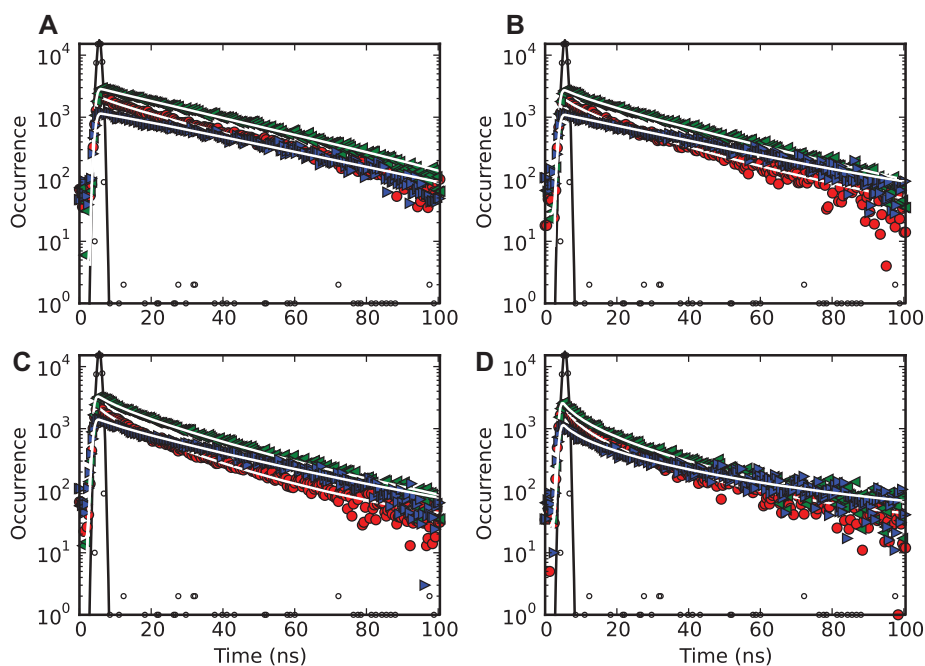


Figure 8 Decay profiles as a function of wavelength for Ems-r2 QDs in an aqueous solution (A), dispersed on the glass substrate (B), on the silver-coated glass substrate (C) and on the hybrid structure (D). Red circles, green left triangles and blue right triangles pertain to decay profiles built 20 nm on the short-wavelength side, at the wavelength, and 20 nm on the long-wavelength side of the emission maximum. The solid white lines are stretched exponential fits of the various decay profiles convoluted with the instrumental response function of the setup (shown in black).

function [8, 9]. In fact, for all types of quantum dots deposited on the hybrid structure, one observes a strong deviation from the single exponential relaxation as a result of the specific various orientations of their transition dipole moments relative to the local polarization of the plasmon-enhanced fields.

The decay rate enhancement of the various QDs is defined as the decay rate measured for the QDs on the hybrid structure divided by the one measured for the QDs on the glass substrate. By proceeding in this way, we rule out the emitter intrinsic properties to focus more directly on the effects induced by interactions with the local environment. Figure 8A shows the evolution of this parameter as a function of wavelength for all different-sized QDs. Very interestingly, all rates are enhanced as the QDs are dispersed on the hybrid structure, since the minimum rate enhancement value exhibited in this plot is 1. Furthermore, in the majority of cases (with the notable exception of the behavior exhibited by Ems-o), all rate enhancements are monotonously increasing functions of the wavelength. Not surprisingly, Ems-g1 (enhancement from 4 to 12) and Ems-r1 (enhancement from 4 to 17), the “bare” CdSe@ZnS QDs, with cores very close to the metal surface (only protected from quenching by the ZnS shell) exhibit a rate enhancement much larger than Ems-g2 (enhancement from 2 to 4) and Ems-r2 (enhancement from 2 to 4), which possess an extra spacing overlayer around the ZnS shell. These observations are compatible with the 14 times emission enhancement reported by Farcau et al. (this number is obtained by taking into account the fact that there are two times more molecules on the corrugated surface area with respect to the flat surface area) [20]. On the contrary, Ems-o exhibits a peculiar rate enhancement behavior with a first increase from 2 to 5 in the range 590–620 nm, followed by a decrease from 5 and back to 1 in the range 620–650 nm.

The experimentally obtained wavelength-dependent rate enhancements exhibited in Figure 9A do not compare with most numerically obtained results, shown in Figure 4, especially in magnitude. A notable exception is the total (radiative+non-radiative parts) Purcell factor exhibited as a function of wavelength for a single emitter (dashed line) located 5 nm in front of the HS and polarized perpendicularly to the metal surface (z-polarized). In this particular case, the agreement in shape and magnitude between the wavelength-dependent rate enhancement F either simulated or measured is remarkable. In particular, the Ems-g1 and Ems-r1 rate enhancements (dashed dark green and dark red lines in Figure 9A) follow extremely closely (from 550 to 600 nm and from 650 to 700 nm, respectively) the simulated increases (as shown by the green and red arrows

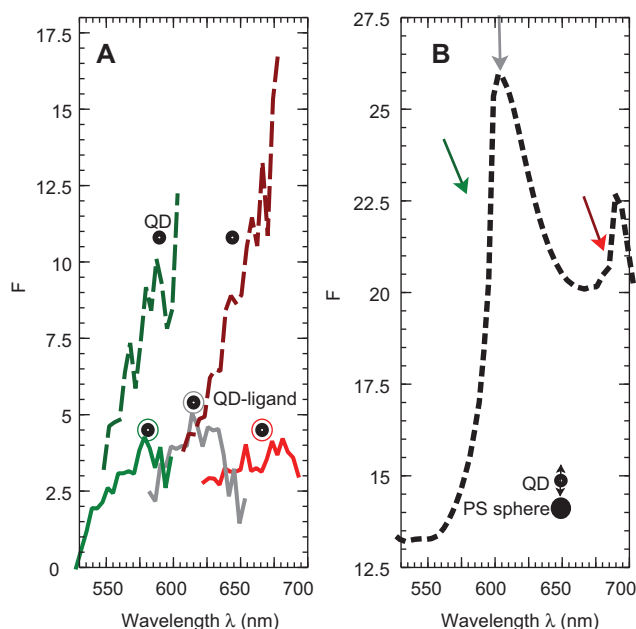


Figure 9 (A) Measured decay rate enhancements for all QDs investigated in this study as a function of the emission wavelength. In all cases, the decay rate of the QDs on the hybrid structure have been divided by the one corresponding to the QDs on the glass substrate (line colors and styles as defined in Figure 2). (B) Simulated decay rate enhancement for a z-polarized emitter located 5 nm in front of the sphere (dashed line).

in Figure 9B). The Ems-g2 and Ems-r2 rate enhancements (solid green and red lines in Figure 9A) follow the same increase as a function of wavelength, while strongly attenuated because of the increased separation of these QDs (having a large overlayer surrounding their cores) from the metal corrugated surface. The Ems-o rate enhancement (gray solid line in Figure 9A), which exhibits a bell shape as a function of wavelength (around 600 nm), also agrees with the behavior of a z-polarized emitter located in front of a HS (as shown by the gray arrow in Figure 9B).

Such a direct comparison between the experimentally obtained rate enhancements (Figure 9A) and Purcell factors F (Figure 4) suggests that we are measuring exclusively emitters located in front of the HSs with a polarization locally perpendicular to the surface of the spheres (Figure 9B). Let us note here that our measurements are performed on the ensemble level, so that none of the experimental decay rate enhancement curves can perfectly match the corresponding (in wavelength) part of F numerically obtained for a single emitter in a particular position and for a particular polarization. Rather, the ensemble result is in general an average signal resulting from the superposition of the signals emitted by several single emitters located at different places with different polarizations, the signal of one emitter being often seen

to dominate over the others [39]. This is the reason for the observation of a remarkable but not excellent matching of the experiments and simulations shown in Figure 9. Furthermore, for the hybrid structure, taking into account the area developed in front of the spheres, it is indeed very probable to find most emitters located there rather than in the V-shaped grooves between the HSs.

To decipher the influence of which mode the emitters are subjected to, it is worthwhile to read the trends shown by the emission rate enhancements with regards to the electric field mode patterns. The Ems-g1 and Ems-g2 QDs are in a wavelength range subjected to the RW mode on the short side and the Bloch-SPP mode on the long side. The larger field amplitude and area covered by this large field in front of the HSs indeed favor a larger interaction strength for emitters subjected to the Bloch-SPP mode (Figure 3). A similar trend is observed for QDs with a large overlayer surrounding them (Ems-g2). The Ems-r1 and Ems-r2 QDs are in the wavelength range of the short-SPP mode towards the LSPP resonance. Their radiative rate enhancements are monotonously increasing functions of wavelength. Once more, the larger field amplitude together with the larger area covered by this field amplitude favor a superior interaction of the emitters located in front of the HSs with the LSPP resonance rather than the short-SPP mode (Figure 3). The Ems-o QDs mainly spectrally overlap the Bloch-SPP mode. They exhibit a bell-shaped radiative rate enhancement, as would do a z-polarized emitter located in front of the HS in this wavelength range. The emission rate enhancement has its maximum in coincidence with the maximum of the Bloch-SPP resonance and is reduced on both sides.

At this level, it is important to emphasize that all Purcell factor wavelength-dependent variations, would it be numerically (total of radiative part of, Figure 4) or experimentally (Figure 9A) investigated, bear the signature of the underlying resonance modes. As such, from a knowledge of the modes exhibited by the hybrid structure, as determined in part A of this paper, we have just shown that we are able to control the wavelength-dependent rate enhancement of emitters chosen appropriately (in size and spectral range) and deposited onto the corrugated surface. From a different perspective, these emitters have been shown to be potential sensors of the resonance modes underlying the electromagnetic properties of the hybrid structure. Such non destructive, very sensitive probes reporting in the far-field the coupling strength (through F) of their near-field interactions with the plasmophotonic modes of the structure can be seen as a future concept for the development of new sensing applications.

4 Conclusions

In conclusion, by inserting various types of QDs in a hybrid structure as nano-reporters of the local interactions between excitons and the plasmophotonic modes of the structure, we were able to control the wavelength-dependent rate enhancements of these QDs owing to two parameters: their spectral overlap with a given mode of the hybrid structure and their relative distance from the structure. Experimentally, we observed that the rates enhancements of the QDs located near the hybrid structure (Ems-g1, Ems-r1) were larger than the ones of the QDs located further away (Emsg2, Ems-o and Ems-r2). Very interestingly, while most QDs exhibit monotonously increasing functions of their rate enhancements with respect to wavelength, the Ems-o shows a bell-shaped dependence. The experimentally measured radiation response is explained according to the enhancement/confinement strength of the involved modes acting on the QDs excitons. All experimental results, including the transmission spectrum of the structure, the rate enhancements of the various QDs and the SPP mode profile recorded by s-SNOM, have been shown to nicely match the appropriate numerical simulations. The chosen nano-reporters have thus been shown to provide a far-field signal able to disentangle the various resonance modes exhibited at the nanoscale level by the hybrid structure. Behind the fundamental importance related to the understanding of the resonance features of the hybrid structures and their effects on nearby emitters, let us strongly emphasize here that the modulation of the resonance features obtained by changing either the diameter of the spheres templates or the thickness of the metal layer straightforwardly opens unlimited applications in the field of fluorescence and bio-fluorescence sensing.

Acknowledgements: The authors thank Emeline Feltrin (CNRS-CRPP, Bordeaux) for having performed the AFM measurements and acknowledge le Conseil Régional d'Aquitaine for the experimental financing support and the allowance of a postdoctoral fellowship to S. Ungureanu. The authors acknowledge the INTERREG IV B SUDOE program of the European Commission through the Train2 project (Trans-Pyrenees Action on Advanced Infrastructures for Nanosciences and Nanotechnology) for funding participation. B. Kolaric acknowledges the financial support from both Smart film grant 830039 (ECV12020020892F) in the framework of the Convergence Project and FNRS. R. Vallée acknowledges FRS-FNRS for a visiting professor grant.

Received February 18, 2013; revised May 28, 2013; accepted June 6, 2013; previously published online June 29, 2013

References

- [1] Lakowitz JR. Principles of fluorescence spectroscopy. Singapore: Springer; 2006
- [2] Asla K, Malyn SN, Zhang Y, Geddes CD. Conversion of just-continuous metallic films to large particulate substrates for metal-enhanced fluorescence. *J Appl Phys* 2008;103:0843071–7.
- [3] Dulkeith E, Ringler MT, Klar A, Feldmann J. [Gold nanoparticles quench fluorescence by phase induced radiative rate suppression.](#) *Nano Lett* 2005;5:585–9.
- [4] Bakker RM, Yuan HK, Liu Z, Drachev VP, Kildishev AV, Shalae VM, Pedersen RH, Gresillon S, Boltasseva A. [Enhanced localized fluorescence in plasmonic nanoantennae.](#) *Appl Phys Lett* 2008;92:043101-3.
- [5] Colas des Francs G, Bouhelier A, Finot E, Weeber JC, Dereux A, Girard C, Dujardin E. Fluorescence relaxation in the near-field of a mesoscopic metallic particle: distance dependence and role of plasmon modes. *Opt Express* 2008; 16:17654–66.
- [6] Carminati R, Greffet JJ, Henkel C, Vigoureux J. [Radiative and non-radiative decay of a single molecule close to a metallic nanoparticle.](#) *Opt Commun* 2006;261: 368–75.
- [7] Chan YH, Chen J, Wark SE, Skiles SL, Son DH, Batteas JD. Using patterned arrays of metal nanoparticles to probe plasmon enhanced luminescence of CdSe quantum dots. *ACS Nano* 2009;3:1735–44.
- [8] Ferrié M, Pinna N, Ravaine S, Vallée RAL. Wavelength-dependent emission enhancement through the design of active plasmonic nanoantennas. *Opt Express* 2011;19: 17697–712.
- [9] Vallée RAL, Ferrié M, Saadaoui H, Ravaine S. Broadband spontaneous emission rate enhancement through the design of plasmonic nanoantennas. *Opt Mat Express* 2012;2: 566–77.
- [10] Maier SA. Plasmonics: fundamentals and applications. New York: Springer; 2007.
- [11] Farcau C, Giloin M, Vinteler E, Astilean S. [Understanding plasmon resonances of metal-coated colloidal crystal monolayers.](#) *Appl Phys B* 2012;106:849–56.
- [12] Romanov SG, Korovin AV, Regensburger A, Peschel U. [Hybrid colloidal plasmonic-photonic crystals.](#) *Adv Mater* 2011;23:2515–33.
- [13] Haynes CL, van Duyne RP. Nanosphere lithography: a versatile nanofabrication tool for studies of size-dependent nanoparticle optics. *J Phys Chem B* 2001;105:5599–611.
- [14] Love JC, Gate BD, Wolfe DB, Paul KE, Whitesides GM. [Fabrication and wetting properties of metallic half-shells with submicron diameters.](#) *Nano Lett* 2002;2:891–4.
- [15] Liu J, Maaroo AF, Wiecek L, Cortie MB. Fabrication of hollow metal nanocaps and their red-shifted optical absorption spectra. *Adv Mater* 2005;17:1276–81.
- [16] Landström L, Brodoceanu D, Piglmayer K, Langer G, Bäuerle D. Infrared transmission through metal-coated lattices of microspheres. *Appl Phys A* 2005;81:15–6.
- [17] Landström L, Brodoceanu D, Piglmayer K, Bäuerle D, Extraordinary optical transmission through metal-coated colloidal monolayers. *Appl Phys A* 2006;84:373–7.
- [18] Zhan P, Wang Z, Dong H, Sun J, Wang HT, Zhu S, Ming N, Zi J. [The anomalous infrared transmission of gold films on two-dimensional colloidal crystals.](#) *Adv Mater* 2006;18:1612–6.
- [19] Landström L, Brodoceanu D, Bäuerle D, Garcia-Vidal FJ, Rodrigo SG, Martin-Moreno L. Extraordinary transmission through metal-coated monolayers of microspheres. *Opt Express* 2009;17:761–72.
- [20] Farcau C, Astilean S. [Silver half-shell arrays with controlled plasmonic response for fluorescence enhancement optimization.](#) *Appl Phys Lett* 2009;95:193110-3.
- [21] Gerber S, Reil F, Hohenester U, Schlagenhaupt T, Krenn JR, Leitner A. Tailoring light emission properties of fluorophores by coupling to resonance-tuned metallic nanostructures. *Phys Rev B* 2007;75:073404-4.
- [22] Kabashin AV, Evans P, Pastkovsky PS, Hendren W, Wurtz GA, Atkinson R, Pollard R, Podolskiy VA, Zayats AV. Plasmonic nanorod metamaterials for biosensing. *Nature Materials* 2009;8:867–71.
- [23] Ament I, Prasad J, Henkel A, Schmachtel S, Sönnichsen C. Single unlabeled protein detection on individual plasmonic nanoparticles. *Nano Lett* 2012;12:1092–5.
- [24] Ocelic N, Huber A, Hillenbrand R. [Pseudoheterodyne detection for background-free near-field spectroscopy.](#) *Appl Phys Lett* 2006;89:101124-6.
- [25] Esteban R, Vogelgesang R, Dorfmueller J, Dmitriev A, Rockstuhl C, Etrich C, Kern K. [Direct near-field optical imaging of higher order plasmonic resonances.](#) *Nano Lett* 2008;8:3155–9.
- [26] Kim DS, Heo J, Ahn SH, Han SW, Yun WS, Kim ZH. [Real-space mapping of the strongly coupled plasmons of nanoparticle dimers.](#) *Nano Lett* 2009;9:3619–25.
- [27] Rang M, Jones AC, Zhou F, Li ZY, Wiley BJ, Xia Y, Raschke MB. Optical near-field mapping of plasmonic nanoprisms. *Nano Lett* 2008;8:3357–63.
- [28] Taflove A, Hagness SC. Computational electrodynamics: the finite-difference time-domain method. Norwood: Artech House Inc.; 2005.
- [29] Oskooi AF, Roundy D, Ibanescu M, Bermel P, Joannopoulos JD, Johnson SG. Meep: a flexible free-software package for electromagnetic simulations by the FDTD method. *Comput Phys Commun* 2010;181:687–702.
- [30] Rakic AD, Djuricic AB, Elazar JM, Majewski ML. Optical properties of metallic films for vertical-cavity optoelectronic devices. *App Opt* 1998;37:5271–83.
- [31] Gao H, McMahon JM, Lee MH, Henzie J, Gray SK, Schatz GC, Odom TW. Rayleigh anomaly-surface plasmon polariton resonances in palladium and gold subwavelength hole arrays. *Opt Express* 2011;17:2334–40.
- [32] Maaroo AF, Cortie MB, Harris N, Wiecek L. Mie and bragg plasmons in subwavelength silver semi-shells. *Small* 2008;4:2292–9.
- [33] Kurokawa Y, Miyasaki H, Jimba Y. [Light scattering from a monolayer of periodically arrayed dielectric spheres on dielectric substrates.](#) *Phys Rev B* 2002;65:201102-5.
- [34] Berini P. Long-range surface plasmon polaritons. *Adv Opt Photon* 2009;1:484–588.
- [35] Stockman MI. Nanofocusing of optical energy in tapered plasmonic waveguides. *Phys Rev Lett* 2004;93:137404–4.

- [36] Agio M. Optical antennas as nanoscale resonators. *Nanoscale* 2012;4:692–706.
- [37] Chen J, Albella P, Pirzadeh Z, Alonso-González P, Huth F, Bonetti S, Bonanni V, Akerman J, Nogués J, Vavassori P, Dmitriev A, Aizpurua J, Hillenbrand R. Plasmonic nickel nanoantennas. *Small* 2011;7:2341–7.
- [38] Novotny L, van Hulst NF. Antennas for light. *Nature Photonics* 2011;5:83–90.
- [39] Kinkhabwala A, Yu Z, Fan S, Avlasevich Y, Müllen K, Moerner WE. Large single-molecule fluorescence enhancements produced by a bowtie nanoantenna. *Nature Photonics* 2009;3:654–7.